Simulations of nuclear pore transport yield mechanistic insights and quantitative predictions

Joshua S. Mincer[a,b] and Sanford M. Simon[a,1]

[a]Laboratory of Cellular Biophysics, Rockefeller University, 1230 York Avenue, New York, NY 10065; and [b]Department of Anesthesiology, Mount Sinai School of Medicine, One Gustave L. Levy Place, New York, NY 10029

Edited by Charles S. Peskin, New York University, New York, NY, and approved May 16, 2011 (received for review March 24, 2011)

To study transport through the nuclear pore complex, we developed a computational simulation that is based on known structural elements rather than a particular transport model. Results agree with a variety of experimental data including size cutoff for cargo transport with (30-nm diameter) and without (<10 nm) nuclear localization signals (NLS), macroscopic transport rates (hundreds per second), and single cargo transit times (milliseconds). The recently observed bimodal cargo distribution is predicted, as is the relative invariance of single cargo transit times out to large size (even as macroscopic transport rate decreases). Additional predictions concern the effects of the number of NLS tags, the RanGTP gradient, and phenylalanine-glycine nucleopore protein (FG-Nup) structure, flexibility, and cross-linking. Results are consistent with and elucidate the molecular mechanisms of some existing hypotheses (selective phase, virtual gate, and selective gate models). A model emerges that is a hybrid of a number of preexisting models as well as a Brownian ratchet model, in which a cargo-karyopherin complex remains bound to the same FG-Nups for its entire trajectory through the nuclear pore complex until RanGTP severs the cargo-Nup bonds to effect release into the nucleus.

mathematical modeling | molecular motor | nuclear-cytoplasmic transport | nucleoporins | filament dynamics

Significant advances in our understanding of the nuclear pore complex (NPC), which mediates all transport between nucleus and cytoplasm, include a cataloging of the structural components, characterization of the transport factors, assays for rates of transport, including measurements of single molecule transit, some preliminary reconstitutions of nuclear transport, structural studies both at the cryo-EM and the X-ray crystallographic level, and molecular dynamics simulations between select components (1).

Qualitative models to explain the selectivity of NPC transport for specifically tagged [nuclear localization signal (NLS)] cargo focus on the roles of the soluble factors and structural components of the pore. Two main soluble factors are Ran and the karyopherins ("kaps," also known as exportins or importins). The kaps are transport receptors that bind with high affinity to NLS cargo, whereas Ran is a small GTPase that exists in a gradient of its GTP:GDP form from the nucleus to cytoplasm and is involved in cargo release. The structural components are flexible filamentous phenylalanine-glycine nucleopore proteins (FG-Nups) that fill the central core of the pore. They are considered relatively "unstructured"—in vitro they lack secondary structure—and they have a series of repeats of the amino acid motif FG, varying from 6 to 43 per filament (2) and of various forms such as FxFG, GLFG, PSFG, or xxFG. All of the FG-Nups are arranged in eightfold symmetry, with some as a single set and some as two or four rings. Although the FG-Nups are essential for selective transport through the nuclear pore, many are dispensable. In yeast, up to 50% of the FG-Nup mass can be deleted while still maintaining cell viability (3).

Despite the progress made in characterizing the nuclear pore complex, there is considerable disagreement on the mechanism for transport, and a number of different hypotheses have been offered. The selective phase model (4, 5) postulates that interactions between FG repeats on different FG-Nups result in the formation of a cross-linked gel. Cargo with an NLS, and in complex with a karyopherin, binds to FG motifs, competing for the FG-FG interactions, thereby allowing the cargo to melt into the gel, enabling transport through repeated steps of binding and melting. The virtual gate model (6) dispenses with the FG-FG interactions, maintaining that the very presence of unstructured FG-Nups prevents passage of cargo lacking a NLS by entropic exclusion. NLS cargo can bind FG-Nups, and this binding energy overcomes the entropic barrier for entering the pore. The competition model (7) maintains that the Nups can exclude cargo lacking an NLS only when cargo with an NLS is present. The reduction-of-dimensionality model (8) maintains that binding of NLS cargo to FG repeats lining the NPC effectively reduces their movement to a two-dimensional random walk, which would be significantly more efficient than the three-dimensional walk experienced by non-NLS cargo. The selective gating/collapse model (9) assumes the virtual gate entropic barrier but maintains that NLS-cargo passage is facilitated by a conformational change of FG-Nups that occurs when binding karyopherins. This binding causes collapse of the bound FG-Nups that reels in the NLS cargo toward the center of the NPC in what is termed "fly casting." It has also been proposed that conformational changes of the entire pore itself result in changes in its effective diameter, helping to facilitate passage of cargo with NLS (10).

It has been previously proposed that nuclear transport may be the consequence of a Brownian ratchet: NLS cargo moving by thermal fluctuations with a chemical potential gradient biasing the net movement (11). However, this model did not specify the molecular mechanism by which the Brownian ratchet may function. Additionally, due to a lack of knowledge of the biophysics and physiology of transport through the pore, the model was not quantified to see if it recapitulated physiologically relevant events including transport rates and transit times.

Although no consensus exists on the mechanism of transport, the accepted experimental detail has reached a level to make the field ripe for simulations to bridge the gap between qualitative ideas and quantitative experiment. Models of nuclear transport take a few forms. Molecular dynamics provide insight into interactions between NPC components (12). However, their time scale (10^{-9}–10^{-6} s) is out of the range of the millisecond transport events. Lower-resolution models of one (13) to three (14) dimensions have replicated specific hypotheses of transport. Here we

Author contributions: J.S.M. and S.M.S. designed research; J.S.M. and S.M.S. performed research; J.S.M. contributed new reagents/analytic tools; J.S.M. and S.M.S. analyzed data; and J.S.M. and S.M.S. wrote the paper.

The authors declare no conflict of interest.

This article is a PNAS Direct Submission.

Freely available online through the PNAS open access option.

[1]To whom correspondence should be addressed. E-mail: simon@rockefeller.edu.

See Author Summary on page 12569.

This article contains supporting information online at www.pnas.org/lookup/suppl/doi:10.1073/pnas.1104521108/-/DCSupplemental.

present a low-resolution yet fully three-dimensional model of NPC transport that can address different transport hypotheses.

In order to capture transport events that occur on the millisecond time scale, we forego the high temporal and spatial resolution of the atomistic approach that is limited to the nanosecond to microsecond time scale and instead opt for a lower-resolution model that nonetheless aims to capture the essential physics and biology of NPC transport. Using simulation to explore relevant parameter spaces, we can then determine under what conditions, if any, the hypothesized mechanisms for transport emerge, whether these conditions are in fact physiologic, and if calculated results agree at least semiquantitatively with experiment. For parameters that have been determined experimentally, such values are employed. For those that are not yet determined, educated guesses are made. Even where parameters have been determined, we aim to vary them by orders of magnitude to explore the sensitivity and robustness of our results to these values. The results recapitulate many of the experimental observations on nuclear transport and demonstrate behaviors consistent with some, but not all, of the proposed models and provide molecular-level detail of how these models may operate.

The Model

Our approach is to create a fully three-dimensional physical space in which to simulate the dynamics of the FG-Nups and cargo with no a priori allegiance to any particular model of transport. We have constructed a model space that includes a single NPC, modeled as a cylinder containing rings of FG-Nup filaments. Although the NPC dimensions may be varied, they are generally 30 nm in length and 50 nm wide, in agreement with the structure of the yeast pore. Additional user-defined space on either side of the NPC completes the model space. A single FG-Nup is modeled as a flexible filament, using the Pairwise Agent Interaction with Rational Superposition (PAIRS) model (15). Filament flexibility is varied primarily through a single parameter (Ctheta); a lone filament anchored at one end to the inside shell of the model NPC cylinder will have different mean end-to-end distances as Ctheta is varied. The amino acid length as well as the filament radius and structure (helix versus extended chain) are varied to yield various FG-Nup structures. FG motifs are modeled as binding sites along the filament length (each structural filament segment is associated with a FG binding site). When FG motifs on the same or different Nups collide, they may bind. Subsequent bond dissociation is governed by a defined FG-FG off rate. Similarly, FG motifs can interact with kap binding sites on the cargo surface when they collide. Individual FG-Nups are anchored in rings of 8-fold symmetry along the NPC length, allowing for variation of the number of such rings as well as the spacing between them.

Cargo is modeled as a spherical molecule of defined diameter. It may have any number of NLS tags, corresponding to an association with a virtual karyopherin represented by FG-binding sites on the cargo surface. Generally, both NLS and non-NLS cargo are introduced in stochastic fashion via a defined rate, thus allowing for competition between the two and determination of selectivity of NLS over non-NLS cargo. RanGTP is introduced into the model in the form of a concentration gradient (maximum at the nucleus) whose shape and magnitude can be defined. Proportional to this concentration (and of actual interest in the model) is the rate at which RanGTP binds the NLS-cargo-kap complex, as this binding displaces the cargo-kap bond (the dissociation of which is exceedingly slow in the absence of RanGTP), with the consequence that the cargo can no longer bind (or rebind) FG-Nups. This displacement occurs whether or not the cargo-kap complex has already bound to FG-Nups (in fact, RanGTP induces a conformational change when binding to the karyopherin, which also affects dissociation, otherwise exceedingly slow, of any kap-FG bonds). See *SI Methods* for greater detail on the model construction. The outcomes generated by the simulations include the macroscopic rates of cargo transport, single cargo transit times, selectivity for NLS versus non-NLS cargo, spatial-temporal distributions of FG-Nups and cargo, and actual analysis of individual trajectories. These are studied as functions of variations in cargo size, number of NLS tags, individual FG-Nup structure (thickness and amino acid length) and dynamics (flexibility), number of FG-Nup filaments, FG-FG off rates, and the RanGTP gradient (Table 1). Details of all of the methodology for the modeling is given in *SI Text*.

Table 1. Parameters varied in the simulations

Parameters varied	Range of values tested in our simulations
Number of rings	1 to 10 rings (8 to 80 FG-Nups; 104 to 2,080 FG repeats)
Spacing between the rings	1.78 to 3.33 nm
FG-Nup filament radius	0.3, 0.6, 1.2, and 3 nm
Ctheta	0.001 to 0.5
Filament amino acid length	150 to 1,800
Number of FG-Nup binding sites per karyopherin	10 (clustered)
Number of FG repeats per filament	13, 26
Off-rate for FG-FG interactions	10^2 to 10^∞/s
Cargo diameter	6 to 48 nm
Ran gradient (distance from center of NPC at which RanGTP falls to 10% of nuclear concentration)	0 to 12.5 nm
Maximum Kap-RanGTP on rate	10^3 to 10^5/s
Width of the NPC	30 to 50 nm
Length of the space for the simulation beyond the 30-nm length of the nuclear pore	70 nm, 120 nm, 170 nm (total length with nuclear pore = 100 nm, 150 nm, 200 nm)

Results

The FG-Nup as Flexible Filament. We first studied the dynamics of a single FG-Nup filament anchored at one of its ends to the inner

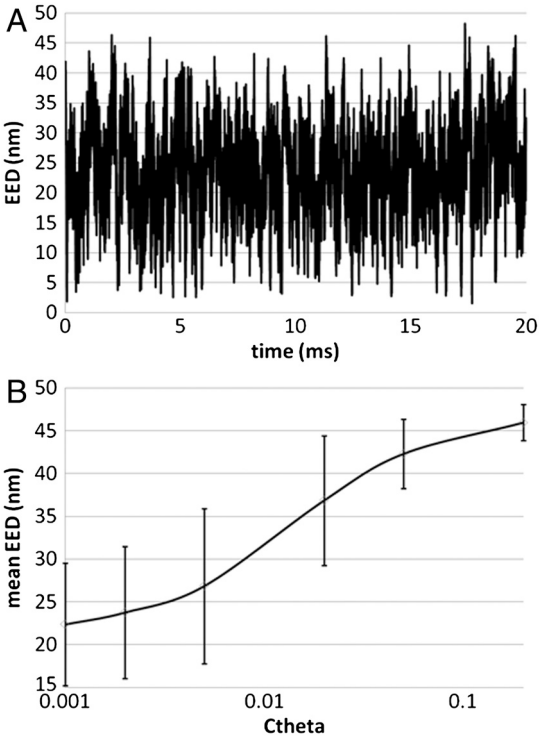

Fig. 1. (*A*) End-to-end distance (EED) dynamics for a single FG-Nup anchored to the inner rim of the model NPC (filament radius 3 nm, length 55 nm, Ctheta = 0.002)

rim of the cylindrical model NPC. A filament of length 55 nm and radius 3 nm (corresponding to approximately 1,800 amino acids), was seen to assume many different conformations of varying end-to-end distances (Fig. 1*A* and Movie S1). Similarly, its free end was seen to transit from one side of the NPC to the other. End-to-end distance was studied as a function of Ctheta (Fig. 1*B*). Decreasing Ctheta increases filament flexibility and decreases mean end-to-end distance. The relationship between Ctheta and mean EED was essentially unchanged when varying filament thickness as well as the number of FG domains.

Populating the NPC with Many FG-Nups. FG-Nup dynamics, cross-linking, and distribution were studied as a function of FG-FG binding by varying the FG-FG off rate for systems of 1 to 10 rings of 8 FG-Nups each for a total of 8 to 80 Nups or a total of 104 to 2,080 FG domains. In the absence of FG-FG interactions (FG-FG off rate = 10^{∞}/s), the filaments were observed to move dynamically from one side of the pore to the other for a 1-ring (Fig. 2*A*, *Top*, Movie S2), a 3-ring (Movie S3), or 10-ring system (80 FG-Nups, Movie S4). The speed and extent of movement was restricted as the FG-FG off rate was slowed (Fig. 2*A*, *Bottom*) from 10^{∞}/s (purple) to 10^{6}/s (green) to 10^{5}/s (red) to 10^{4}/s (blue) for the 1-ring (Fig. 2*B Left*, Movie S5), 3-ring (Movie S6), and 10-ring systems (Fig. 2*B*, *Right*, Movie S7). The observations were similar for off rates of 10^{5}/s or faster. Analysis of the bonds between FG-Nups (Fig. 2*C*) revealed extensive linkage for off rates slower than 10^{5}/s and few bonds for faster off rates.

The FG-FG off rate modulated the FG-Nup dynamics. At one end of this continuum ($<10^{4}$/s), dynamics emerged that were reminiscent of the selective phase model, a cross-linked gel. At the other end of the spectrum ($>10^{5}$/s), the dynamics resembled the virtual gate model. The 10^{5}/s off rate is a transition in which there was a gel-like cross-linking, although looser and of greater spatial extent than denser, more cohesive gels found at lower off rates.

Evidence for the Brownian Ratchet: The RanGTP/RanGDP Gradient Is Necessary for Transport For a nuclear pore devoid of FG-Nups or RanGTP, 10-nm diameter cargo transported at approximately 280 particles/s (Fig. 3*B*, yellow line). In the presence of a single ring of noninteracting FG-Nups (i.e., FG-FG interactions turned off), cargo without an NLS transited the pore at 80 particles/s (Fig. 3*B*, black line); for three or more rings of FG-Nups, 10-nm diameter cargo did not transit at all (the non-NLS size cutoff was smaller, i.e., 6 nm, as in Figs. S1 and S2). Cargo with and without an NLS were stochastically introduced to a pore with FG-Nups present but lacking RanGTP. Transport of either cargo was zero (Fig. 3*B*, purple line). This was a consequence of the karyopherin/FG-Nup off rate (<1/s; see *SI Methods*). The pore was jammed with NLS cargo, preventing other cargo from transiting. There was no net transport in the absence of a gradient of RanGTP:RanGDP.

A gradient of RanGTP was introduced as a Gaussian function decreasing from the nuclear to cytoplasmic side (Fig. 3*A*). As described in *SI Methods*, a particular gradient is characterized

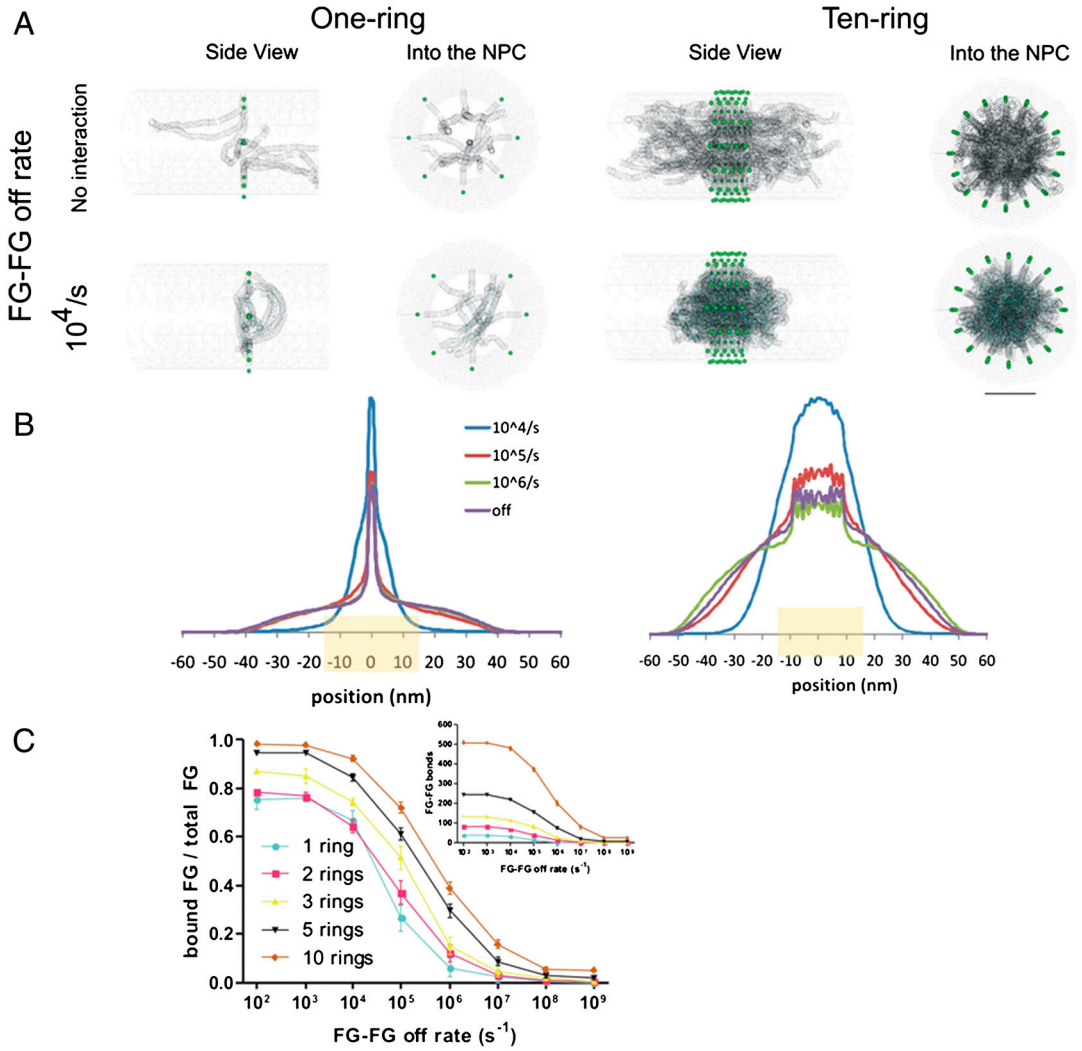

Fig. 2. FG-Nup interactions and dynamics as a function of FG-FG off rate. (*A*) Snapshots of FG-Nup dynamics looking at a side view of the NPC (from within the plane of the nuclear membrane) or into the NPC (from the cytosol or nucleus), for FG-FG off rate 10^{4}/s and for no FG-FG interactions. Scale bar is 30 nm. (*B*) FG repeat domain density histograms for a variety of FG-FG off rates. The beige box marks the thickness of a NPC. (*C*) The fraction of FG repeat domains that are bound to other FG repeat domains and absolute number of FG-FG bonds (*Inset*) as a function of FG-FG off rate for different FG-Nup landscapes.

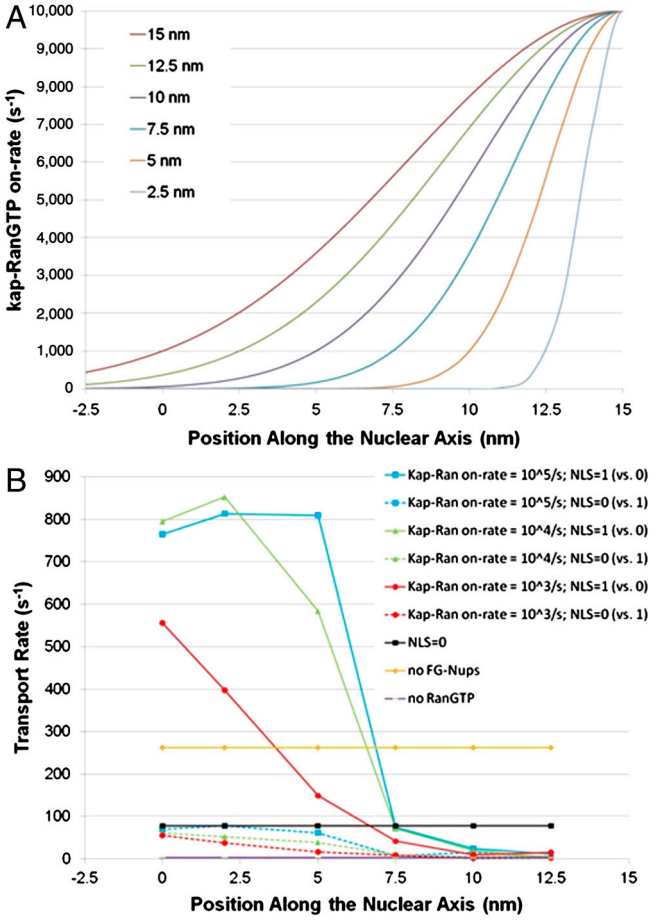

Fig. 3. Effects of varying the RanGTP gradient. (*A*) Gradients of different width for maximum kap-RanGTP on rate of 10^4/s. Maximum [RanGTP], and hence maximum kap-RanGTP on rate, occurs at the nucleoplasmic entrance to the NPC, at position +15 nm along the nuclear axis. Wider gradients penetrate farther in that [RanGTP], and hence the kap-RanGTP on rate, falls to 10% of the maximum closer to the center of the NPC (position 0). For example, the red curve corresponds to a width of 15 nm because the on rate falls to 10% at position 0. (*B*) Effects on transport rates for one NLS versus zero cargo (10-nm diameter) simultaneously introduced into the pore (compare solid and dashed lines of the same color) for the various RanGTP gradients in the 1-ring system, no FG-FG interactions, and Ctheta = 0.02. Each point corresponds to a different RanGTP gradient: The maximum kap-RanGTP on rate is indicated by the color, as defined in the legend, whereas the gradient width is indicated by the x-axis value, as in *A*; i.e., the position along the nuclear axis at which [RanGTP] falls to 10% of its maximum. Also graphed are the rate of zero NLS cargo alone (black line), the rate in the absence of RanGTP (purple line) (illustrated for zero NLS cargo and identical to the rate for the competing one NLS cargo), and the rate in the absence of FG-Nups (yellow line).

by two parameters: the maximum kap-RanGTP on-rate (representing the RanGTP concentration at the nucleoplasmic side) and the width of the gradient, in particular the position along the nuclear axis (cytoplasm = −15 nm, NPC center = 0 nm, nucleus = +15) at which the RanGTP concentration (and hence kap-RanGTP on rate) drops to one-tenth of the maximum value found at the nucleoplasmic side. The cyan, green, and red curves in Fig. 3*B* correspond to gradients with maximum kap-RanGTP on rates of 10^5/s, 10^4/s, and 10^3/s, respectively. Each point in each of these curves corresponds to a gradient of different width, derived from the point's x-axis value, as described in the figure legend.

The presence of a RanGTP gradient accelerated the rate of transport of cargo with one NLS (the solid cyan, green, and red curves in Fig. 3*B*) to levels even faster than transport in the absence of FG-Nups (Fig. 3*B*, yellow line). Increasing the maximum kap-RanGTP on rate increased the rate of transport, although increasing the maximum on rate above 10^4/s had little effect (compare cyan, green, and red solid curves in Fig. 3*B*). Allowing RanGTP to diffuse further into the pore affected the transport rate as well, with wider gradients (i.e., moving to the left on the x axis in Fig. 3*B*) generally yielding increased transport rates. However, when RanGTP penetrated too far into the pore, the simulation predicted a decrease in the transport rate (i.e., rate decreases when moving from 2.5 to 0 nm along the x axis for both the cyan and green solid curves). This decrease is a consequence of the RanGTP releasing some cargo-NLS-karyopherin complexes from the FG-Nups on the cytoplasmic side of the pore.

Cargo with and without a single NLS were introduced simultaneously and stochastically into the pore (compare solid and dashed lines of corresponding color) in order to allow for competition between them (see *SI Methods*). When RanGTP minimally diffused into the pore (i.e., positions 7.5 to 12.5 nm along the x axis), NLS cargo bound the FG-Nups essentially irreversibly and transport of NLS and non-NLS cargo was blocked (solid and dashed curves approach zero rate). When RanGTP entered farther into the pore (position 5 nm and below along the x axis), there was transport of NLS-containing cargo and competition with the non-NLS cargo was reduced (dashed lines approach black line, i.e., the rate of 0 NLS cargo alone). The on rates of RanGTP also affected competition. Specifically, as the on rate increased from 10^3/s to 10^5/s, the transport of cargo without an NLS increased (compare dashed cyan, green, and red curves in Fig. 3*B*).

These results support the rudimentary Brownian ratchet model. Namely, cargo moves with a filament in the pore by thermal fluctuations. The gradient of RanGTP concentration decreasing from the nucleoplasmic to cytoplasmic side of the NPC is necessary to release the cargo from the filament, ratcheting the cargo on the nuclear side, resulting in NLS-cargo transport. Simulation in the model NPC allows for even finer resolution, currently unavailable through experiment, which elucidates an actual mechanism for the Brownian ratchet.

A Molecular Mechanism for the Brownian Ratchet Model Emerges in Analysis of Single Cargo Trajectories. The transit of individual cargo molecules was followed with 1 (Movie S8), 3 (Fig. 4, Fig. S3 *B* and *C*, and Movies S9, S10, and S11), and 10 rings (Movie S12) of FG-Nups (Fig. S3*A*). All simulations were run with an equal concentration of cargo with and without a NLS. Irrespective of variation in FG-FG interactions, number of filaments, filament flexibility (i.e., Ctheta), or dynamics of RanGTP interactions, the behavior of cargo with an NLS was similar under all conditions and could be described by five phases.

Both NLS and non-NLS-cargo approach the NPC by thermal fluctuations. Phase 1 begins when NLS cargo first binds (is captured by) an FG-Nup. Once one binding site on a cargo-bound karyopherin binds an FG-Nup, subsequent sites rapidly (<0.2 ms) bind other FG domains, most on the same filament (blue line in Fig. 4*B* and Fig. S3), but occasionally on other filaments (red and green lines). The cargo-NLS-karyopherin moves by thermal fluctuations. However, with each additional bond between the karyopherin and an FG domain, the cargo is pulled deeper into the NPC. Thus, in phase 1, cargo moves in a directed manner as if reeled in by the filament (black line in Fig. 4*B* and Fig. S3). This movement resembles fly casting and is accomplished by the FG-Nups rapidly binding sites on the karyopherin, winding around and effectively shortening in length, potentially accounting for the FG-Nup collapse observed by Lim et al. (9).

Phase 2 initiates once the cargo-NLS-karyopherin binds all of its FG-binding sites. This phase is marked by two behaviors. First, the cargo fluctuates in the pore from thermal motion, but constrained by its bonds to the filaments (note limited Δposi-

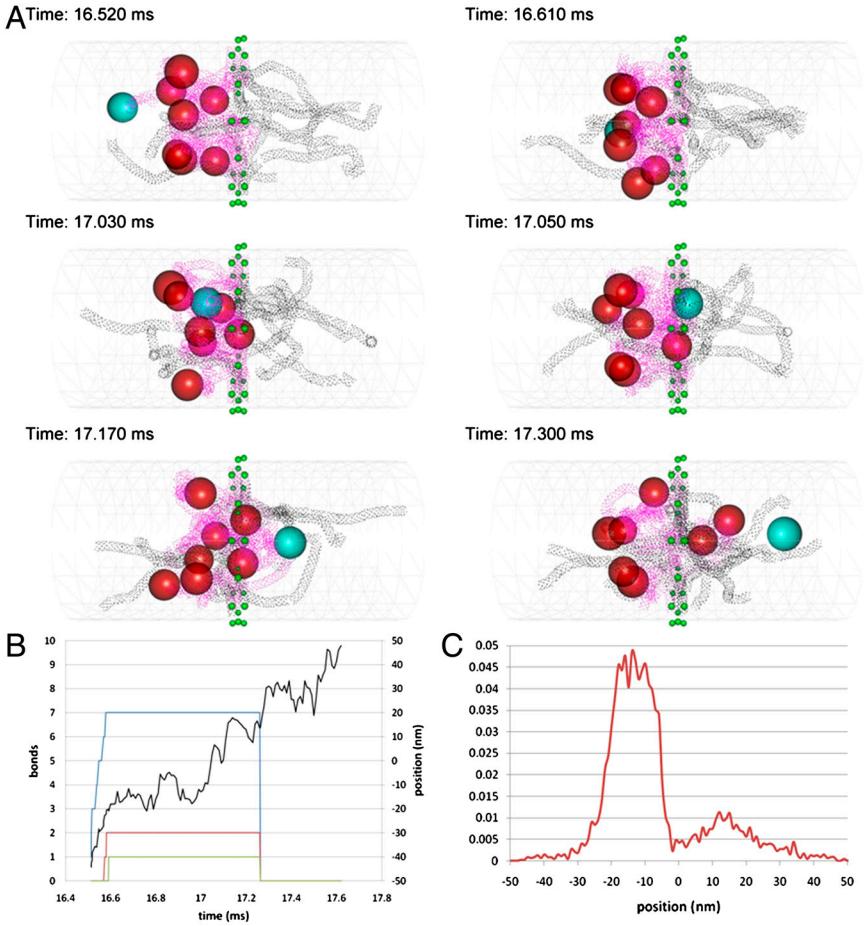

Fig. 4. Analysis of cargo trajectories. (*A*) Snapshots from the trajectory of a 10-nm diameter cargo with one NLS (green sphere) in the 3-ring system (no FG-FG interactions, Ctheta = 0.02) (red sphere = other NLS cargo; pink filaments are bound to NLS cargo). (*B*) Quantitative analysis of the highlighted (green) trajectory in *A*: The black curve indicates the position over time, whereas each of the other curves represents the number of bonds between the cargo and a particular FG-Nup. (*C*) Histogram from combined transporting cargo trajectories, illustrating the cargo position density (i.e., probability of finding a single cargo at a given position).

tion from 16.6 to 17 ms for the cargo in Fig. 4*B*, from 3 to 8 ms for the cargo in Fig. S3*A*, from 4.5 to 10.5 ms for the cargo in Fig. S3*B*, and from 9.125 to 9.25 ms for the cargo in Fig. S3*C*). The second behavior is the surrounding unbound FG-Nups, through thermal fluctuations, slowly enveloping the cargo-NLS-karyopherin and reorganizing around it. The cargo thus spends time around 10–15 nm from the center on the cytoplasmic side.

In phase 3, the FG-Nups have reorganized and present less of a barrier to movement of the cargo to the nucleoplasmic side. The cargo can move by thermal fluctuations from its relatively stable point on the cytoplasmic side to an equivalent stable position on the nucleoplasmic side of the central core of the FG filaments. This FG-Nup reorganization is consistent with the virtual gate/entropic exclusion model and in fact provides the molecular mechanism by which it operates. Non-NLS cargo cannot bind FG-Nups; consequently, most will diffuse back out of the NPC before FG-Nups reorganize around them to enable passage through the NPC.

In phase 4, the cargo fluctuates around this stable point until its karyopherin binds RanGTP, enabling release and subsequent movement by thermal fluctuation away from the NPC (phase 5). In the absence of RanGTP, the particle fluctuates back and forth from its position in phase 2 to that of phase 4. Because waiting for FG-Nup reorganization and waiting for RanGTP binding are the slowest parts of transport, cargo is predicted to spend most of its time in either phase 2 or phase 4, confirmed by the spatial cargo distribution plotted in Fig. 4*C*. This bimodal distribution is in agreement with recent single molecule experiments, published while this paper was in review (16). Throughout, cargo is bound primarily to one or at most a few FG-Nups until its release by RanGTP. The robustness of this mechanism is demonstrated in the 10-ring system, where despite the large density of FG-Nups seen by the approaching cargo, it nonetheless is bound to the same three filaments throughout its translocation of the NPC (Fig. S3*A*); most of those bonds are in fact associated with one particular filament.

The mechanism elucidated here is consistent with the Brownian ratchet model: Namely, NLS cargo moves by thermal motion through the NPC, and transport can occur only in the presence of a RanGTP gradient. It furthermore offers unique insights as to how the ratchet works. The free ends of FG-Nups in fact transit from one side of the pore to the other through thermal motion. An NLS cargo is seen to bind one, or at most a few, FG-Nups on the cytoplasmic side of the NPC, to which it remains bound for its entire transit through the NPC. Neighboring FG-Nups must reorganize around the cargo-Nup complex, and this is in fact a rate-limiting step that, together with time spent waiting for RanGTP release, rationalizes the predicted bimodal spatial-temporal cargo distribution. In the absence of RanGTP, the cargo-Nup complex diffuses back and forth repeatedly. However, in the presence of a gradient of RanGTP, contact with RanGTP severs the cargo-Nup and cargo-kap bonds and allows for release to the nucleoplasmic side. Although RanGTP was proposed earlier to act in some fashion as a Brownian ratchet, the transport mechanism that emerges in these simulations demonstrates how this actually occurs and as such constitutes a detailed explanation for how it operates. In fact, these simulations also delineate molecular mechanisms for the other consistent transport models: FG-Nup reorganization explains the virtual gate/entropic exclusion model, and the hypothesized fly casting of the selective gate/collapse model is clearly seen.

Brownian Ratchet Predicts Cargo Size Cutoffs and Transport Rate Variation. When the FG-Nups were omitted from the pore (Fig. 5*A*, purple boxes), there was a weak size dependence for cargo to successfully transit the pore. Macroscopic transport rates were

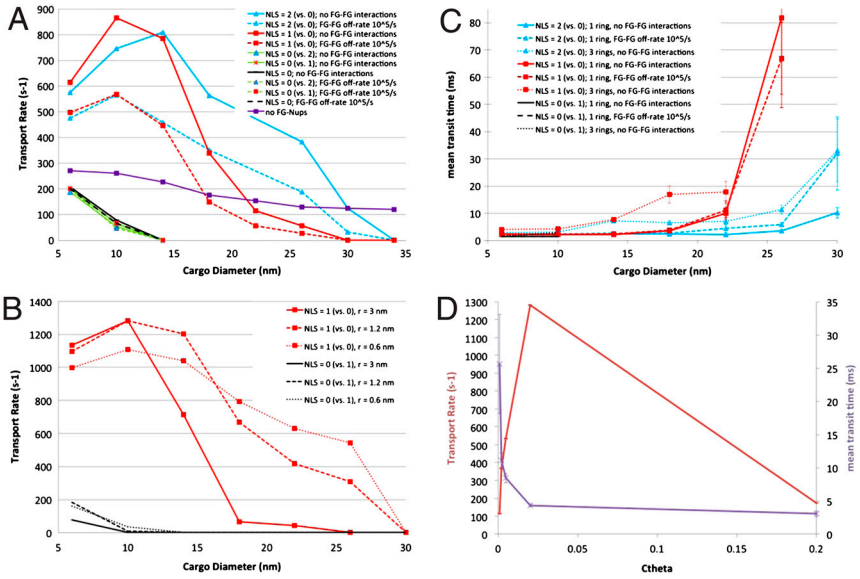

Fig. 5. Cargo dynamics: macroscopic transport rates (*A*, *B*, and *D*) and mean transit times (*C* and *D*) as a function of cargo size and number of NLS tags for different FG-FG off rates (*A* and *C*) and FG-Nup structure (r = FG-Nup filament radius) (*B*) and flexibility (Ctheta) (*D*). Results for *A* were produced in the 1-ring system, whereas those for *B* and *D* are from the 3-ring system (*C* features results from both). Unless otherwise specified, Ctheta = 0.02. FG-FG interactions are varied in *A* and *C* and turned off in *B* and *D*.

on the order of 280/s for 6-nm diameter cargo and a little over 100/s for 34-nm diameter cargo. Introducing the eight FG-Nups into a single ring reduced the size of non-NLS cargo that transited the pore below 10-nm diameter (Fig. 5*A*, black lines; the non-NLS size cutoff decreases to 6 nm with increasing number of rings of FG-Nups, i.e., Figs. S1 and S2 and with decreasing pore diameter, i.e., Fig. S4). Cargo with and without a single NLS were introduced into pores with [RanGTP] decreasing to 10% at the NPC center. Cargo with a single NLS (red lines) transited the pore at rates exceeding 800/s, and cargo up to 26-nm diameter (the size of a ribosome) could now transit the nuclear pore complex. When cargo containing two NLS was introduced, even larger cargo (up to 30-nm diameter) could readily transit the pore (cyan lines). In each case the macroscopic transport rates and size selectivity of cargo without an NLS were barely affected by the presence of NLS cargo (compare black and green lines). These trends held with 1, 3, or 10 rings of FG-Nups, as well as for varying distances between these rings (Figs. S1 and S2).

Selective Phase Dynamics (FG-FG Cross-Linking) Decreases Transport Rate. To test for effects of FG-FG interactions on transport, the FG-FG bond off rate was varied (Fig. 5). Cargo up to 18-nm diameter (one NLS) and 26-nm diameter (two NLS) successfully transported through the pore at least as fast in the presence of FG-Nups as it did through an empty pore devoid of FG-Nup filaments. The fastest rate of transport occurred in the absence of interactions between the FG groups on the Nups (k_{off} for FG-FG interactions = 10^{∞}). Slowing the k_{off} between the filaments slowed the rate of transport of NLS-containing cargo (Fig. 5*A*, compare FG-FG off rate of 10^5/s, dashed lines, and 10^{∞}/s, solid lines). This decreased transport was observed with two NLS (cyan line, Fig. 5*A*) or one (red line, Fig. 5*A*). For cargo without an NLS, there was no detectable effect of varying the FG-FG off rate on the rate of transport (compare green lines). These trends held for FG-Nups of varying flexibility (compare Fig. 5*A* and Fig. S5). Increasing filament flexibility (decreasing Ctheta and EED) generally decreased transport rate, though the relationship is more complex (see below).

Brownian Ratchet Predicts That FG-Nup Structure Effects Transport Rate. In addition to results for 3-nm radius FG-Nup filaments (17, 18) shown throughout, we also studied 1.2-nm radius filaments, 0.6-nm radius (an alpha helix), and 0.3-nm radius (an extended peptide chain) (Fig. 5*B* and Fig. S2), all of the same static length. As described in *SI Methods*, this corresponds to filaments ranging between 150 and 1,800 amino acids. Results for different thickness filaments were qualitatively similar. Quantitatively, thinner diameter FG-Nups allowed a faster transport rate for larger NLS-containing cargo and a slightly slower rate for smaller cargo (Fig. 5*B*). The Brownian ratchet model not only predicts this variation but also explains it: Owing to their smaller cross-sectional area, thinner filaments are less efficient at capturing incoming NLS cargo but are more efficient at reorganizing around it and each other. As such, thinner filaments yield a slightly diminished transport rate at lower cargo size, where the discrepancy in capturing cargo dominates. Larger cargo, owing to its larger cross-sectional area, will be captured by filaments of essentially any thickness. Consequently, thinner filaments yield increasing transport rates owing to their greater efficiency at reorganization. Trends delineated above for FG-FG interactions as well as increasing number of NLS tags held for the thinner filaments, as demonstrated in Fig. S2 and Table S1.

Brownian Ratchet Predicts Single Molecule Transit Times. Histograms were generated for the transit times for individual cargo molecules (Fig. S6; 10-nm diameter cargo, NLS = 1, Ctheta = 0.02) and the mean transit time plotted as a function of the cargo size and the number of NLS (Fig. 5*C*). The mean transit time is relatively unchanged over a large range of cargo sizes even as macroscopic transport rate decreases, a prediction recently verified in a paper published while this manuscript was in review (19). For cargo >18-nm diameter, there was a substantial increase in the transit time. The presence of two NLS decreased the mean transit time, especially for larger cargo (diameter ≥26 nm) for which the transit time with one NLS was long enough that experimentally it might not be observed to transit the pore. These simulations of transit times are on the millisecond time scale, in agreement with recent single molecule measurements (20, 21). Stabilizing the FG-FG cross-linking by decreasing the FG-FG off rate (10^5/s) slowed transport rate (see Fig. 5*A* and Fig. S5) and increased mean transit time. For the 10-ring system (Table S2), stabilizing FG-FG interactions slowed transport rate by >50% (325 to 114/s) and increased the mean transit time by approximately 33% (27 to 35 ms). Note that individual non-NLS-cargo molecules transited faster than NLS cargo, a prediction that has also been verified while this manuscript was in review (19), representing the fact that free diffusion around FG-Nups is faster than transport mediated by binding to the Nups. NLS cargo, after all, is slowed down by the actual events of binding and RanGTP-mediated unbinding. Thus, exclusion of

individual non-NLS cargo is a consequence of the low probability of such transport occurring, not the time scale of such transit when it does in fact occur.

As mentioned above, the low probability of non-NLS-cargo transport is explained by the Brownian ratchet molecular mechanism: A non-NLS cargo, not being bound to FG-Nups, is likely to diffuse back out to the cytoplasm in the time it takes for neighboring FG-Nups to reorganize around it (phase 2 of the Brownian ratchet mechanism delineated above). Similarly, cargo with two NLS transits faster and with increased macroscopic rate compared to cargo with one tag. More bonds between two NLS cargo and bound FG-Nups stabilizes its position relative to one NLS cargo, which compared with two NLS cargo is more of a moving target. Reorganization of neighboring FG-Nups around the more stationary two NLS cargo is therefore more efficient.

Effects of Varying the Flexibility of the FG-Nup Filaments Are Explained by the Brownian Ratchet Mechanism. Ctheta is a parameter that tunes the flexibility of individual filaments. Lowering Ctheta results in individual filaments with smaller end-to-end distance. Ctheta was varied from 0.001 to 0.2, corresponding to end-to-end distances from 22 ± 7 nm to 46 ± 2 nm (Fig. 1*B*). The mean transit time decreases with decreased flexibility (increased Ctheta) (Fig. 5*D*, purple line). The dependence of transport rate on Ctheta is more complicated (Fig. 5*D*, red line), with a maximum occurring at intermediate flexibility. The reasons for these relationships become clear from observing the trajectories of individual cargo (compare Movies S9, S10, and S11 and corresponding Fig. 4*B* and Fig. S3 *B* and *C*) that illustrate the Brownian ratchet molecular mechanism. More rigid filaments extend further, contact an individual cargo earlier in its trajectory, and reel in the cargo more quickly (Fig. S3*C*, black line). This accounts for the decrease in mean transit time of a single cargo molecule, i.e., phase 1 of the Brownian ratchet mechanism is faster. However, owing to its stiffness, a rigid filament (with a high Ctheta) takes longer to "reset," i.e., to return to a position at which it can bind a new cargo. Put another way, the translocation of FG-Nup free ends through the pore by Brownian motion is slower for the stiffer filaments. This results in less efficiency and an overall decrease in macroscopic transport rate. Optimization of these opposing trends gives the maximum transport rate at intermediate Ctheta, as seen in Fig. S3*C*. Comparing Movie S10 and Fig. S3*C* also explains why, for Ctheta = 0.2, the cargo seems to linger (though for a relatively short time) on the nucleoplasmic side once released by RanGTP binding (Fig. S3*C*). Namely, diffusion of the cargo away from its release point is momentarily hindered by the many surrounding stiff filaments that have yet to reset to the cytoplasmic side of the NPC.

Discussion

Numerous models have been proposed to explain selective transport across the nuclear pore. There has been little progress in resolving between these models for two reasons. First, the models are not formulated in a manner that allows them to make quantitative predictions that can be falsified. This quantification is essential for resolving between a model that might be "possible" but insufficient to account for physiological observed rates. Second, many of them have not been formulated in sufficient biophysical detail to make it possible to evaluate molecular mechanism. Recent significant advances in the ability to make biophysical measurements of the transit times and rates of single cargo provide information that can be used to test these models, if they are properly formulated. Our computational model of the NPC, created without a priori fidelity to a particular hypothesized mechanism, provides a quantitative tool for testing these models and yields results that are in agreement with different experimental data and provide insight into the molecular mechanisms underlying transport.

Based on these results, it is possible to draw some conclusions regarding the utility of competing models. Macroscopic transport rate was seen to increase as one moved from FG-FG off rates of $\leq 10^5$/s [resembling the selective phase (4, 5)] to faster off rates [resembling the virtual gate model (6)]. Without knowing the true FG-FG off rate inside of the NPC, it is not possible to say which model better approximates dynamics of the FG-Nups in the NPC. Recent applications of fluorescence anisotropy to the NPC offer the potential for resolving the dynamics of the FG-Nups (22, 23). However, even in the absence of such information, we can conclude that the higher-level cross-links of the selective phase mechanism are not required to explain NPC transport. That is, doing away entirely with FG-FG interactions not only maintains selectivity in transport but in fact increases overall rates of transport of NLS cargo. Thus, it is not necessary to invoke FG-FG interactions to account for the rates or selectivity of transport. The Brownian ratchet model, which emerges in the analysis of single cargo trajectories, provides an explanation for this result. FG-FG cross-linking prolongs phase 2 of transport, the FG-Nup reorganization around transiting cargo, and as such slows transport.

The "competition model" (7) is tested throughout by simultaneously introducing both NLS and non-NLS cargo into the pore. Over the wide range of conditions tested, the presence of FG-Nups alone was sufficient to limit non-NLS transport. Thus it is entropic exclusion by FG-Nup filaments (the virtual gate) that is sufficient to exclude non-NLS cargo and ensure selectivity of the NPC. Generally in our simulations, NLS cargo was seen to limit transport of non-NLS cargo only under nonphysiologic conditions, specifically only in the presence of nonphysiologic RanGTP gradients that also severely limited NLS cargo.

The computer simulations are most consistent with a hybrid of some of the existing models: the virtual gate (entropic exclusion), selective gate (collapse/fly casting), selective phase, and Brownian ratchet models. In fact, analysis of single cargo trajectories generated in these simulations actually reveals molecular mechanisms for these models. The Brownian ratchet model, demonstrated here in molecular detail, initially proposed that NLS cargo diffuses through the NPC until it is released by RanGTP (the Brownian ratchet) on the nucleoplasmic side (11). Thermal ratchets were initially proposed as a "thought experiment" that would lead to a perpetual motion machine (review in ref. 24). The term Brownian ratchet was coined to describe how a molecular motor, working in a realm whose motion is dominated by Brownian motion, can take advantage of thermal motion and a chemical potential gradient to do work (11). The Brownian ratchet was applied earlier to the movement of molecules across membranes, in particular the endoplasmic reticulum (11) although it was suggested to apply to transport of macromolecules across other membranes including transport through the nuclear pore (11). Recently, a Brownian ratchet was invoked to explain nuclear export (25). This formulation was not sufficiently detailed to allow it to be quantitatively tested. The detailed mechanism of transport that emerges in our simulations finally enables understanding of a mechanism for a Brownian ratchet model. Namely, RanGTP severs the bonds between NLS cargo and the FG-Nup (or few FG-Nups) to which it remains bound and transits with together throughout its motion in the NPC. Without this release, the cargo-Nup complex would diffuse back and forth repeatedly.

A Brownian ratchet model provides a solution to previously puzzling aspects of nuclear transport. Many of the proposed models, (i.e., selective phase and reduction of dimensionality) require multiple rounds of karyopherin-FG-Nup binding/unbinding during each transport event. However, the observed nanomolar dissociation constant for the kap-FG bond (corresponding to an off rate of 1/s or less) with multiple rounds of binding and unbinding would take many orders of magnitude longer than the observed millisecond transport rates. The Brownian ratchet

model posits that there are no unbinding events during transport, thus avoiding the problem of the apparently slow dissociation rate of karyopherin from the FG-Nup. Whichever FG-Nup filament the cargo binds to, it remains bound to until it reaches the nucleoplasmic side of the nuclear pore and is released by RanGTP (see Fig. S7).

Other aspects of NPC transport are similarly naturally explained by the molecular mechanism underlying the Brownian ratchet model. The flexibility of FG-Nups is thought to be central to their function. In the Brownian ratchet model, this flexibility is obviously necessary for FG-Nup/cargo translocation across the pore, enabling FG-Nups to bind NLS cargo and transit with it until being released by RanGTP. Flexibility is furthermore necessary for the reorganization of neighboring FG-Nups around transiting NLS-cargo-Nup complexes.

Recent experimental data that are not readily explained by other models are predicted and explained by the Brownian ratchet mechanism discovered here. The bimodal spatial-temporal distribution of NLS cargo is predicted by the cargo-Nup complex waiting for neighboring FG-Nups to reorganize (waiting at the cytoplasmic side) and then waiting for RanGTP to bind (waiting at the nucleoplasmic side) (phases 2 and 4 of the Brownian ratchet molecular mechanism). This polymer reorganization around a FG-Nup bound cargo molecule is a physical embodiment of the virtual gate model. This result of pausing on one side, not obvious in other models, is quantitatively predicted in our simulations and was confirmed in experiments published while this paper was in review (16). The FG-Nup reorganization that is central to the Brownian ratchet mechanism explains a variety of phenomena (described above), including why FG-FG cross-linking central to the selective phase model actually slows down transport and why two NLS cargo is faster than one NLS cargo. It also explains the result predicted in our simulations and confirmed while our paper was in review (19) that out to relatively large cargo size, the mean transit time of individual NLS cargo is essentially constant (Fig. 5*C*). The slow step of reorganization is a characteristic of the FG-Nups themselves and not of the transiting cargo (and therefore not of the cargo's size).

Interestingly, the Brownian ratchet mechanism allows for some rapprochement between the virtual gate and selective phase models. In these simulations the microenvironment in the pore is dominated by the density of FG-Nups, whether or not they are in the gel (cross-linked) state posited by the selective phase model. Cargo molecules that do not bind to a filament will not freely diffuse through, as posited by the "entropic exclusion" model. Once the cargo is bound to a filament, the other filaments slowly reform, or reorganize, around it—the transiting NLS cargo can be viewed as a melting into and through this FG-Nup polymer. Thus, the lowering of energy for entropic exclusion is the result of the polymers reforming around it, allowing the cargo to melt through the FG-Nup polymers. In this way FG-Nup reorganization is reminiscent of the melting that occurs in the selective phase model while not requiring that model's posited cycles of binding and unbinding of NLS cargo to FG repeats to melt the existing FG-FG bonds. Not only does transport not require a gel-like state (where a gel implies cross-linking), but our results in fact demonstrate that cross-linking between the polymers, far from facilitating NLS-cargo transport, actually hinders it.

Our simulations provide a molecular mechanism for the Brownian ratchet model and elucidate the molecular mechanisms of the virtual gate model and selective gate model (fly casting) while providing predictions to guide further study. Discussed above, these include the extent of RanGTP diffusion into the NPC, quantitative comparison of NLS cargo with different numbers of NLS tags, experimental determination of the effects of FG-FG cross-linking on transport (predicted here to slow it down), and effects of varying FG-Nup structure and flexibility. The latter may be particularly important in light of the recent proposal that FG-Nups of distinct structure types are distributed in a nonrandom way within the pore (26). The central tenet of the Brownian ratchet model molecular mechanism elucidated in our simulations, that a cargo molecule remains bound to the same FG-Nups throughout its trajectory through the NPC, has yet to be verified experimentally.

ACKNOWLEDGMENTS. We acknowledge Jonathan Alberts for making publicly available the ParMSpindle code and for helpful discussions further elucidating the structure and function of that code. We thank the members of the Laboratory of Cellular Biophysics, especially Daniel Johnson, Claire Atkinson, and Alexa Mattheyses, as well as Elias Coutavas and Martin Kampmann, for ongoing discussions, and J.S.M. further acknowledges Sahrena London, Guiseppe Narzisi, and Dimitri Antoniou for helpful conversations. Support is acknowledged from the Eliasberg Clinical Scientist Training Program in the Department of Anesthesiology of the Mount Sinai School of Medicine (to J.S.M.) and from the National Institutes of Health Grant GM87977 (to S.M.S.).

1. Lim RY, Ullman KS, Fahrenkrog B (2008) Biology and biophysics of the nuclear pore complex and its components. *Int Rev Cell Mol Biol* 267:299–342.
2. Peters R (2009) Translocation through the nuclear pore: Kaps pave the way. *BioEssays* 31:466–477.
3. Strawn LA, Shen T, Shulga N, Goldfarb DS, Wente SR (2004) Minimal nuclear pore complexes define FG repeat domains essential for transport. *Nat Cell Biol* 6:197–206.
4. Frey S, Richter RP, Gorlich D (2006) FG-rich repeats of nuclear pore proteins form a three-dimensional meshwork with hydrogel-like properties. *Science* 314:815–817.
5. Ribbeck K, Gorlich D (2002) The permeability barrier of nuclear pore complexes appears to operate via hydrophobic exclusion. *EMBO J* 21:2664–2671.
6. Rout MP, Aitchison JD, Magnasco MO, Chait BT (2003) Virtual gating and nuclear transport: The hole picture. *Trends Cell Biol* 13:622–628.
7. Jovanovic-Talisman T, et al. (2009) Artificial nanopores that mimic the transport selectivity of the nuclear pore complex. *Nature* 457:1023–1027.
8. Peters R (2005) Translocation through the nuclear pore complex: Selectivity and speed by reduction-of-dimensionality. *Traffic* 6:421–427.
9. Lim RY, et al. (2007) Nanomechanical basis of selective gating by the nuclear pore complex. *Science* 318:640–643.
10. Melcak I, Hoelz A, Blobel G (2007) Structure of Nup58/45 suggests flexible nuclear pore diameter by intermolecular sliding. *Science* 315:1729–1732.
11. Simon SM, Peskin CS, Oster GF (1992) What drives the translocation of proteins? *Proc Natl Acad Sci USA* 89:3770–3774.
12. Miao L, Schulten K (2009) Transport-related structures and processes of the nuclear pore complex studied through molecular dynamics. *Structure* 17:449–459.
13. Zilman A, Di Talia S, Chait BT, Rout MP, Magnasco MO (2007) Efficiency, selectivity, and robustness of nucleocytoplasmic transport. *PLoS Comput Biol* 3:e125.
14. Kustanovich T, Rabin Y (2004) Metastable network model of protein transport through nuclear pores. *Biophys J* 86:2008–2016.
15. Alberts JB (2009) Biophysically realistic filament bending dynamics in agent-based biological simulation. *PLoS ONE* 4:e4748.
16. Grunwald D, Singer RH (2010) In vivo imaging of labelled endogenous beta-actin mRNA during nucleocytoplasmic transport. *Nature* 467:604–607.
17. Delphin C, Guan T, Melchior F, Gerace L (1997) RanGTP targets p97 to RanBP2, a filamentous protein localized at the cytoplasmic periphery of the nuclear pore complex. *Mol Biol Cell* 8:2379–2390.
18. Walther TC, et al. (2001) The nucleoporin Nup153 is required for nuclear pore basket formation, nuclear pore complex anchoring and import of a subset of nuclear proteins. *EMBO J* 20:5703–5714.
19. Tu LC, Musser SM (2010) Single molecule studies of nucleocytoplasmic transport. *Biochim Biophys Acta*, 10.1016/j.bbamcr.2010.12.011.
20. Sun C, Yang W, Tu LC, Musser SM (2008) Single-molecule measurements of importin alpha/cargo complex dissociation at the nuclear pore. *Proc Natl Acad Sci USA* 105:8613–8618.
21. Dange T, Grunwald D, Grunwald A, Peters R, Kubitscheck U (2008) Autonomy and robustness of translocation through the nuclear pore complex: A single-molecule study. *J Cell Biol* 183:77–86.
22. Mattheyses AL, Kampmann M, Atkinson CT, Simon SM (2010) Fluorescence anisotropy reveals order and disorder of protein domains in the nuclear pore complex. *Biophys J* 99:1706–1717.
23. Kampmann M, Atkinson CE, Mattheyses AL, Simon SM (2011) *Nat Struct Mol Biol*, 18 pp:643–649.
24. Feynman R, Leighton R, Sands M (1963) *The Feynman Lectures on Physics* (Addison-Wesley, Reading, MA).
25. Stewart M (2007) Ratcheting mRNA out of the nucleus. *Mol Cell* 25:327–330.
26. Yamada J, et al. (2010) A bimodal distribution of two distinct categories of intrinsically-disordered structures with separate functions in FG nucleoporins. *Mol Cell Proteomics* 9(10):2205–2224.

Supporting Information

Mincer and Simon 10.1073/pnas.1104521108

SI Methods

General Considerations in Modeling the Nuclear Pore Complex (NPC). Our approach is to create a fully three-dimensional physical space in which to simulate the dynamics of the phenylalanine-glycine nucleopore proteins (FG-Nups) and cargo with no a priori allegiance to any particular model of transport. We have generated a model space that includes a single NPC, modeled as a cylinder containing rings of FG-Nup filaments. In the simulation, cargo molecules—with or without nuclear localization signals—are introduced into the model space. The filaments are allowed to fluctuate and to interact with each other and with the cargo. The outcomes generated by the simulations are the macroscopic rates of cargo transport, single cargo transit times, selectivity for NLS versus non-NLS cargo, spatial-temporal distributions of FG-Nups and cargo, and actual analysis of individual trajectories. These are studied as functions of variations in cargo size, number of nuclear localization signal (NLS) tags, individual FG-Nup structure (thickness and amino acid length) and dynamics (flexibility), number of FG-Nup filaments, FG-FG off rates, and the RanGTP gradient (Table 1).

In order to capture transport events that occur on the millisecond time scale, we forego the high temporal and spatial resolution of the atomistic approach that is limited to the nanosecond to microsecond time scale and instead opt for a lower resolution model that nonetheless aims to capture the essential physics and biology of NPC transport. Using simulation to explore relevant parameter spaces, we can then determine under what conditions, if any, the hypothesized mechanisms for transport emerge, whether these conditions are in fact physiologic, and if calculated results agree at least semiquantitatively with experiment. For parameters that have been determined experimentally, such values are employed. For those that are not yet determined, educated guesses are made. Even where parameters have been determined, we aim to vary them by orders of magnitude to explore the sensitivity and robustness of our results to these values.

Software. The starting point for development of our software was the ParMSpindle Java code of Jonathan Alberts (Center for Cell Dynamics, University of Washington). This code implements the PAIRS model (1) for filament dynamics (see below), a Brownian diffusion model, and a basic binding scheme for filament-filament and filament-spherical particle interaction in a closed 3D space. Upon this model we have made some additions and modifications, as follows.

Basic Behavior of Filament. Repulsion forces were added so that filaments could not pass through one another.

Binding of Filament. The intrinsic "side-bonding" scheme, which was important for filaments studied by Alberts, was modified to allow interactions with the FG domains on the filamentous FG-Nups. These interactions include binding between the FG domains on different FG-Nups, between the FG domains on the same FG-Nup, binding between the FG-Nup and a binding site on the karyopherin (cargo) binding, and competition among all three. The binding between the filaments and particle was modified to recapitulate the known binding between the FG-Nup and karyopherins. Specifically, each karyopherin had discrete clustered binding sites. The karyopherin binding sites could interact along the entire length of the FG-Nup filament (not just at the ends as in the original formulation).

Orientation and Anchoring of Filaments. The geometry of the FG-Nup filaments was constrained to model the arrangement in the NPC. Specifically, each FG-Nup was anchored at one end around the inside of a ring with eightfold symmetry. Different numbers of rings of FG-Nups and differing interactions between FG-Nups enable the generation of FG-Nup landscapes (see Fig. 2). The movement of the filaments, the binding interactions between the filaments, and the movement of cargo and its interactions with the FG-Nups are defined within this space. Potential transport molecules are stochastically introduced at one end of this space. Some of these contain NLS and some do not, allowing the study of their relative transport rates.

NPC Geometry. The NPC is modeled as a cylinder of user-defined diameter and length. For the experiments described here, a length of 30 nm and diameter of 50 nm were chosen to model the yeast NPC (2). However, some results are presented with a diameter of 30, 40, and 50 nm. Note that when the diameter is set at 50 nm, the effective diameter is actually closer to 40 nm as a consequence of the space occupied by FG-Nups. The model space extends beyond the NPC dimensions to form a cylinder of total length 100 nm. This allows for exploration of FG-Nup dynamics and interaction with cargo that can extend beyond the NPC dimensions. Both the number of rings of FG-Nups as well as the spacing of the rings within the model NPC was varied.

FG-Nups. A single FG-Nup is largely disorganized and flexible (3), enabling it to be modeled as a flexible filament. The PAIRS model of Jonathan Alberts was employed, which divides filaments into rigid segments on which all relevant forces (Brownian, segment-segment, etc.) act in pairwise fashion (1). Segments are linked by translational and torsional springs, and the characteristics of the filament of the whole emerge from tuning these springs. One of the few studies on the flexibility of an FG-Nup used atomic force microscopy to yield a persistence length of cNup153 to be about 0.4 nm (4), a value significantly lower than most other biological filaments that are on the order of tens of nanometers or much greater. End-to-end distance is a measurement that is related to persistence length in that both will be shorter in a more flexible filament. However, with an FG-Nup filament anchored at one end, the "persistence length" may vary along the length of the filament. Thus, we used the end-to-end distance as a more natural quantity to measure in our model NPC. We are able to generate filaments of different end-to-end distances by tuning the PAIRS torque attenuation Ctheta that attenuates the torque between filament segments. A smaller Ctheta results in greater filament flexibility and a shorter end-to-end distance (Fig. S1).

A single FG-repeat domain is represented by a binding region on each filament segment that can interact with other FG-repeat domains and with NLS cargo. In particular, a single FG-Nup was modeled as having 150 to 1,800 amino acids (5, 6) with 13 or 26 FG-repeat domains spaced along its length [vertebrate FG-Nups have between 6 and 43 repeats; the 13-repeat Nup is one of the most prevalent (7)]. A given length filament can correspond to different FG-Nup structures. For example, an alpha-helix has a radius/thickness of 0.6 nm and a translation of 0.15 nm along the helical axis. A 55-nm alpha-helix would thus correspond to a peptide of length 370 aa. An extended chain peptide has a thickness of 0.3 nm and a translation of 0.361 nm/residue. Thus a 55-nm extended chain corresponds to 150 aa. Because the in vivo structures of FG-Nups are not well known, we study these as well as others. Specifically, we consider a filament of radius 3 nm,

similar to that of resolved cytoplasmic (i.e., RanBP2) and nucleoplasmic (i.e., vertebrate Nup153) Nups (8, 9). A 55-nm filament of radius 3 nm would correspond to approximately 1,800 aa, whereas that of 1.2-nm radius (also considered here) would be approximately 730 aa. When not explicitly noted, results are for the 1,800 aa filament.

FG-Nup Landscape and Dynamics. To model a population of FG-Nups in the NPC, individual FG-Nup filaments are anchored in rings of 8-fold symmetry along the NPC length. The number of FG-Nups per ring, number of rings, and interring distance are user-defined. The results presented here all used eight copies of the FG-Nups per ring, but include 1-ring (8 FG-Nups; 104 FG-repeat domains), 3-ring (24 FG-Nups; 512 FG-repeat domains), and 10-ring (80 FG-Nups, 1040 FG-repeat domains) landscapes. The 10-ring system is close to the value of 100 FG-Nups that are believed to occupy the central core of the channel (10). Additionally, the distance between the rings was varied in the work presented here from 1.78 to 3.33 nm.

FG-FG Binding. When filament segments collide, they repel each other. However, if each has a free FG-repeat domain in the collision zone, they can bind each other. Dissociation of the FG-FG bond is governed by a user-defined off rate. The K_d for FG-FG interactions ranges between 5 and at least 70 μM (11). The on rate, however, is unknown. Employing the diffusion-limited on rate of 10^7–10^9/M*s results in a range for the off rate from 50/s to at least 70,000/s. Given this uncertainty, in examining the dynamics of the FG-Nup we varied the off rate over a range of seven orders of magnitude, as well as turning off FG-FG interactions (binding) altogether (k_{off} for the FG-FG interactions is instantaneous, i.e., 10^{∞}/s).

Cargo Structure and Binding. Cargo molecules are modeled as spheres of defined diameter. Cargo may have any number (or zero) NLS tags. To model the association of each NLS with a karyopherin, clustered karyopherin (kap)-FG binding sites are mapped to the cargo sphere surface. Within the model, it is possible to model different clustering schemes. For this study, the karyopherin was modeled with 10 FG binding sites clustered on a 5-nm diameter ring [to approximate the clustering found in recent molecular dynamics simulations (12)]. This is mapped onto the cargo sphere at each karyopherin position (thus, the size of a given molecule transiting the pore is the size of the cargo plus its associated karyopherins). Cargo can bind FG-repeat domains when collision occurs if the FG-repeat domain is free and the cargo has a binding site in proximity. The affinity of an individual karyopherin-FG bond has been measured in a variety of experiments to be in the nanomolar range (13, 14). Assuming a diffusion-limited on rate of 10^7–10^9/M-s, this puts the off rate around 1/s (likely an upper limit because the on rate is likely lower). For most simulations presented here, the kap-FG off rate in the absence of RanGTP is set to 1/s. However, it has been varied. See Fig. S7 for a schematic illustrating the cargo-kap-FG binding scheme.

Cargo Dynamics. The same underlying diffusion model generates appropriate Brownian forces for both FG-Nup filament segments and cargo molecules. The model allows one to stochastically generate fluxes for both NLS and non-NLS cargo by specifying each flux's arrival rate (representing a constant concentration outside of the NPC). To examine either an NLS or non-NLS flux alone, this rate may be zero. For the simulations presented, a total arrival rate of 10,000/s cargo molecules was chosen (5,000/s with an NLS and 5,000/s without). The starting position for the cargo molecule along the length of the NPC is also specified and is generally at −45 nm from NPC center (whereas the NPC cytoplasmic entrance is at −15 nm). To test if cargo of larger diameter might have a higher probability of capture because their surface started closer to the FG-Nup filaments, the simulations were repeated with cargo started at 45, 70, and 95 nm from the NPC center. Because the results were indistinguishable, only the results from starting the cargo at 45 nm from the NPC are presented. The position of the cargo in the yz plane is randomized. In the course of its dynamics, cargo that exits back out the entrance side (at −50 nm) is counted as reflected, whereas cargo that exits the other way (i.e., makes it to position +50 nm) is counted as transported. Cargo-FG interaction may occur anywhere along the 100-nm model length.

RanGTP Gradient (Effect on kap-Cargo and kap-FG Dissociation). The off rate for the karyopherin-FG bond is orders of magnitude slower (1/s) (14) than the observed millisecond cargo transit times (15). Similarly, the spontaneous karyopherin-cargo off rate (in the absence of RanGTP) is exceedingly slow (10^{-4}/s to 10^{-3}/s) (16). However, RanGTP binds karyopherin allosterically, inducing a fast conformational change on the order of tens of nanoseconds (17, 18), effectively instantaneous for these simulations, which both enables the bound RanGTP to actively displace bound cargo from kap as well as to effect dissociation of kap from any bound FG repeats (19). Thus, in these simulations, once RanGTP has displaced kap from cargo, the cargo cannot bind (or rebind) FG-repeat domains. RanGTP binding to the cargo-kap complex can occur whether or not the complex is bound to FG-repeat domains. A concentration gradient is maintained across the NPC, with RanGTP in the nucleus at least 200 times in excess of that in the cytoplasm (20). This gradient gives directionality to cargo import by favoring dissociation of kap-cargo complexes on the nucleoplasmic side of the NPC. The measured on rate for RanGTP binding to karyopherin is less than 10^5/M-s (21, 22), too slow to allow for millisecond transit times for the micromolar concentration of RanGTP in the nucleus. Other factors (Nup1p, Nup2p) have been found to accelerate this rate (16). Additionally, the localized concentration of RanGTP at the nucleoplasmic exit may be greater than that measured in the bulk of the nucleus as a consequence of binding of RanGTP to specific Nups.

Ran-Gradient (Shape). Based on the above, the effective kap-RanGTP on rate as a function of position along the NPC axis is not known. Using this simulation, it is possible to vary both the shape of the RanGTP concentration gradient and the size of the gradient across the pore. We have varied the RanGTP concentration gradient as a single step function and a series of steps. In the work presented here we have modeled the RanGTP concentration within the NPC as a Gaussian, with its maximum at the nucleoplasm exit (+15 nm and onward) and minimum at the cytoplasm entrance (−15 nm and onward) (Fig. 3*A*). In the simulations presented, the position in the pore at which the RanGTP falls to 1/10th of its nuclear concentration is varied (see *Results*). Choosing a maximum effective kap-RanGTP on rate at position +15 nm (i.e., the point of maximum RanGTP concentration), the off rate within the NPC is assumed to be proportional to the RanGTP concentration and therefore also varies as a Gaussian function of position.

Simulations. Initialization consists of generating the appropriate filament landscape at time zero. An equilibration time (generally 1 ms) then allows for equilibration of the organization of the FG-Nup filaments. Cargo then enters stochastically according to the specified arrival rates. An integration step of 2 ns is employed as it was seen to produce FG-nup dynamics that converged (produced equivalent FG-repeat density histograms and fraction of bound FG repeats, as in Fig. 2) for a 1-ns as well as a 0.1-ns time step (when steps were increased to 5 ns, convergence was lost). In general, a total run time is specified (generally 0.5 s), after which

the simulation concludes. Along the way, relevant statistical measures are calculated and written to files.

Data Analysis.

Most of the analysis was done during the course of simulation. Some analysis was done postsimulation with MSExcel and Prism GraphPad.

FG-Repeat Density Histograms. The x coordinate of each FG-repeat domain segment is stored at a user-defined interval (generally every microsecond). A histogram with 1-nm binning is then generated by integrating over all FG-repeat domains over a total specified time and normalized by the total number of positions measured in that time. The resulting histogram represents average FG-repeat domain density as a function of position along the length of the model space. For the 1-ring histograms, data from four simulations was collected, where positions were stored every microsecond for 19 ms following a 1-ms equilibration time. For the 10-ring histograms, data from 10 simulations were collected, and positions were similarly stored for 400 ms following 100-ms equilibration time. Equilibration times varied because they depend on the number of FG-FG bonds.

FG-FG Bond Dynamics. The total number of FG-FG bonds was stored every 10 ns over 400 ms, following 100-ms equilibration time. Data were fitted to give mean and standard deviation.

Macroscopic Rate of Transport. In addition to monitoring the arrival cargo fluxes, the absolute number of cargo reflected or transported is recorded over time. For the latter, the result can generally be fitted to a straight line, the slope of which is the macroscopic transport rate. Data are reported as rate and standard error.

Mean Transit Time. Residence (transit) times are recorded for all cargo molecules that transit through the NPC. The mean and standard error are calculated for each distribution.

Cargo-FG Bond Trajectory. Once a cargo molecule binds any FG-repeat domain, a file is opened for its cargo-FG bond trajectory. In particular, the number of bonds from that cargo to each filament is recorded every 10 ms or whenever the bonding changes (whichever is sooner). Also recorded is the x coordinate of the cargo center of mass. From these data, the number of bonds to each filament as either a function of time or cargo position can be plotted.

Cargo Position Histogram. The x coordinates stored in individual transported cargo trajectories are combined, and the resulting distribution is used to generate a 1-nm binned histogram. This represents the average probability of finding cargo at a particular position.

Calculation of End-to-End Distance. A single FG-Nup filament was anchored to the inner rim of the model NPC. The end-to-end distance was recorded over time, from which the mean and standard devation were derived.

Movies. Trajectories can be stored at intervals to generate files that can be played back in a viewer incorporated into the software. This allows for qualitative understanding as well as for generating JPG files that can be converted to movie formats.

1. Alberts JB (2009) Biophysically realistic filament bending dynamics in agent-based biological simulation. *PLoS ONE* 4:e4748.
2. Alber F, et al. (2007) The molecular architecture of the nuclear pore complex. *Nature* 450:695–701.
3. Krishnan VV, et al. (2008) Intramolecular cohesion of coils mediated by phenylalanine—Glycine motifs in the natively unfolded domain of a nucleoporin. *PLoS Comput Biol* 4:e1000145.
4. Lim RY, (2006) Flexible phenylalanine-glycine nucleoporins as entropic barriers to nucleocytoplasmic transport. *Proc Natl Acad Sci USA* 103:9512–9517.
5. Stoffler D (2003) Cryo-electron tomography provides novel insights into nuclear pore architecture: Implications for nucleocytoplasmic transport. *J Mol Biol* 328:119–130.
6. Sun C, Yang W, Tu LC, Musser SM (2008) Single-molecule measurements of importin alpha/cargo complex dissociation at the nuclear pore. *Proc Natl Acad Sci USA* 105:8613–8618.
7. Peters R (2009) Translocation through the nuclear pore: Kaps pave the way. *BioEssays* 31:466–477.
8. Delphin C, Guan T, Melchior F, Gerace L (1997) RanGTP targets p97 to RanBP2, a filamentous protein localized at the cytoplasmic periphery of the nuclear pore complex. *Mol Biol Cell* 8:2379–2390.
9. Walther TC, et al. (2001) The nucleoporin Nup153 is required for nuclear pore basket formation, nuclear pore complex anchoring and import of a subset of nuclear proteins. *EMBO J* 20:5703–5714.
10. Rout MP (2000) The yeast nuclear pore complex: Composition, architecture, and transport mechanism. *J Cell Biol* 148:635–651.
11. Patel SS, Belmont BJ, Sante JM, Rexach MF (2007) Natively unfolded nucleoporins gate protein diffusion across the nuclear pore complex. *Cell* 129:83–96.
12. Isgro TA, Schulten K (2007) Cse1p-binding dynamics reveal a binding pattern for FG-repeat nucleoporins on transport receptors. *Structure* 15:977–991.
13. Ben Efraim I, Gerace L (2001) Gradient of increasing affinity of importin beta for nucleoporins along the pathway of nuclear import. *J Cell Biol* 152:411–417.
14. Pyhtila B, Rexach M (2003) A gradient of affinity for the karyopherin Kap95p along the yeast nuclear pore complex. *J Biol Chem* 278:42699–42709.
15. Yang W, Gelles J, Musser SM (2004) Imaging of single-molecule translocation through nuclear pore complexes. *Proc Natl Acad Sci USA* 101:12887–12892.
16. Gilchrist D, Mykytka B, Rexach M (2002) Accelerating the rate of disassembly of karyopherin.cargo complexes. *J Biol Chem* 277:18161–18172.
17. Zachariae U, Grubmuller H (2008) Importin-beta: Structural and dynamic determinants of a molecular spring. *Structure* 16:906–915.
18. Lee SJ, Matsuura Y, Liu SM, Stewart M (2005) Structural basis for nuclear import complex dissociation by RanGTP. *Nature* 435:693–696.
19. Otsuka S, Iwasaka S, Yoneda Y, Takeyasu K, Yoshimura SH (2008) Individual binding pockets of importin-beta for FG-nucleoporins have different binding properties and different sensitivities to RanGTP. *Proc Natl Acad Sci USA* 105:16101–16106.
20. Kalab P, Weis K, Heald R (2002) Visualization of a Ran-GTP gradient in interphase and mitotic Xenopus egg extracts. *Science* 295:2452–2456.
21. Gorlich D, Seewald MJ, Ribbeck K (2003) Characterization of Ran-driven cargo transport and the RanGTPase system by kinetic measurements and computer simulation. *EMBO J* 22:1088–1100.
22. Saric M, et al. (2007) Structural and biochemical characterization of the Importin-beta.Ran.GTP.RanBD1 complex. *FEBS Lett* 581:1369–1376.

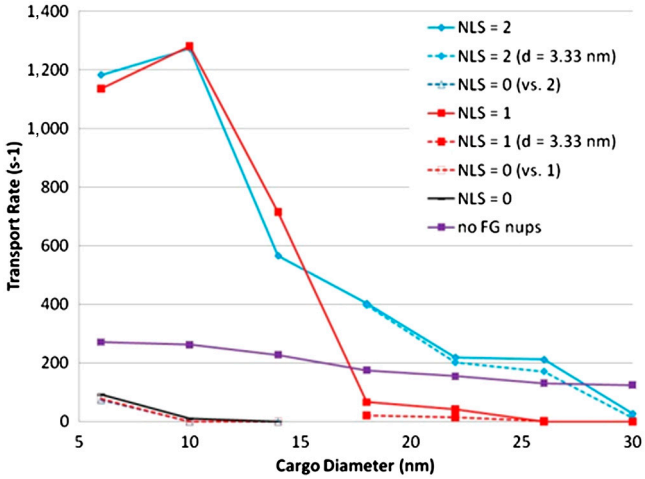

Fig. S1. Macroscopic transport rates for the 3-ring system (Ctheta = 0.02, no FG-FG interactions) as a function of cargo size and number of NLS tags. Unless noted, the interring distance is 1.78 nm; also shown are the data for distance 3.33 nm (a 10-ring system with the latter spacing would fill the entire length of the NPC and as such represents an upper limit).

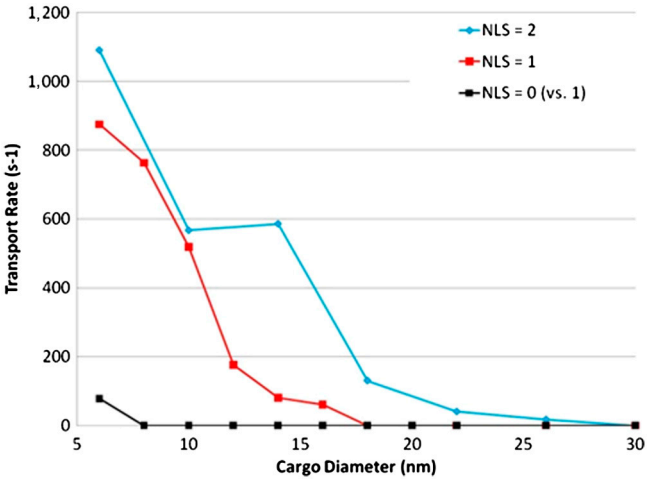

Fig. S2. Macroscopic transport rates for the 10-ring system as a function of cargo size and number of NLS tags (FG-Nup filament radius = 0.3 nm, Ctheta = 0.002, no FG-FG interactions).

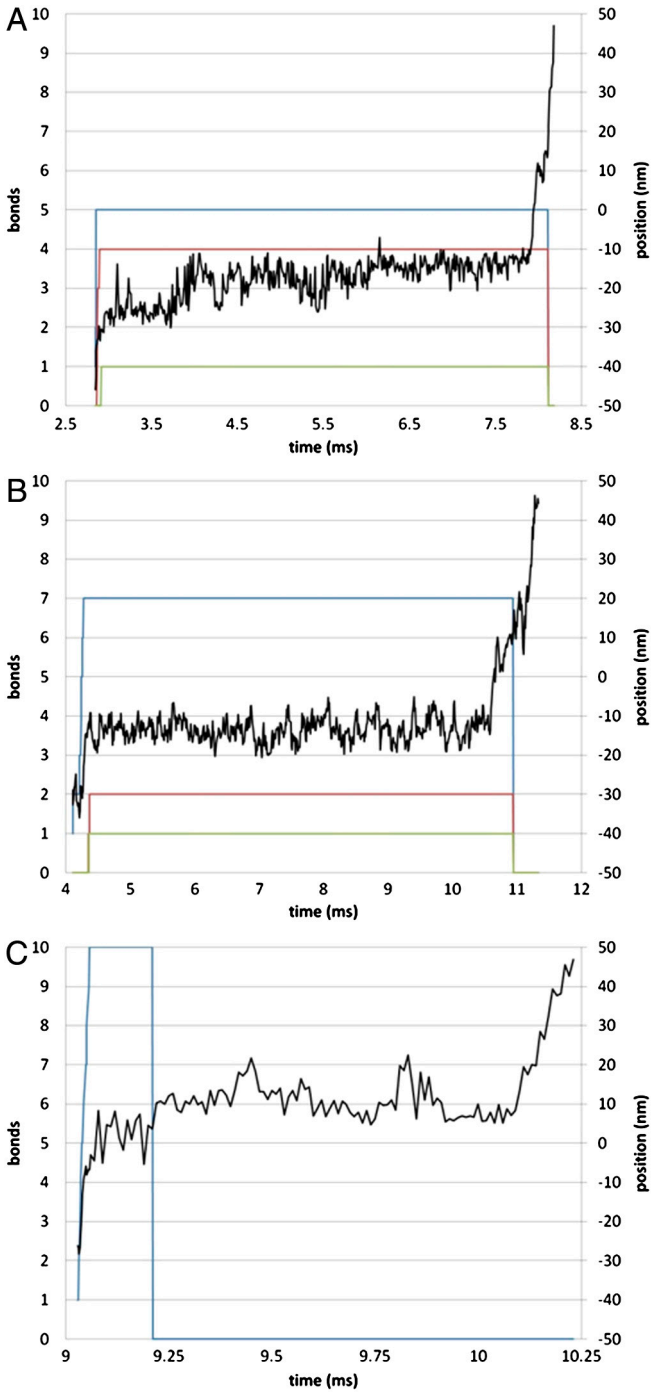

Fig. S3. Analysis of individual cargo trajectories. (*A*) Quantitative analysis of a trajectory for a 10-nm diameter cargo with one NLS in the 10-ring system (no FG-FG interactions, Ctheta = 0.02). (*B*) Quantitative analysis of a trajectory for a 10-nm diameter cargo with one NLS in the 3-ring system (no FG-FG interactions, Ctheta = 0.002). (*C*) Quantitative analysis of a trajectory for a 10-nm diameter cargo with one NLS in the 3-ring system (no FG-FG interactions, Ctheta = 0.2).

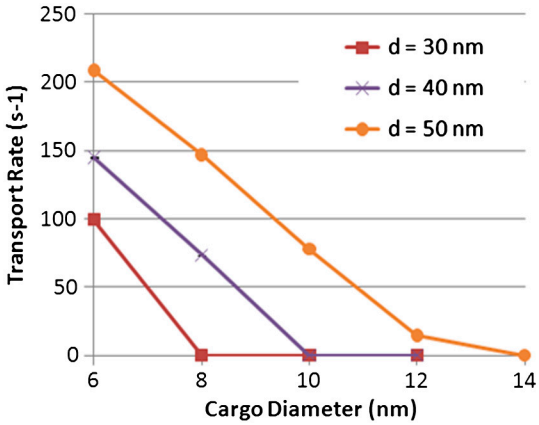

Fig. S4. Effect of varying the width of the NPC. Rates of transport for non-NLS cargo as a function of size of the NPC (1-ring system, no FG-FG interactions, Ctheta = 0.02, FG-Nup radius 3 = nm); *d* = NPC diameter. All of the studies described within the text were done with an interior diameter for the relatively static components of the NPC of 50 nm. The relatively "disordered" FG-Nups penetrated inward to the lumen of the pore. We varied the interior diameter from 30 to 50 nm, in part because the actual static interior diameter is still not resolved and because there have been suggestions that the interior diameter may not be static (1). Varying the size of the pore affected the size of the cargo that could permeate the pore: For an internal static diameter of 30 nm, the largest non-NLS cargo that could permeate had a diameter of 6 nm, with 40 nm, the largest was 8 nm, and with 50 nm the largest was 10 nm. Otherwise there were no significant qualitative differences observed in the simulations.

1. Melcak I, Hoelz A, Blobel G (2007) Structure of Nup58/45 suggests flexible nuclear pore diameter by intermolecular sliding. *Science* 315:1729–1732.

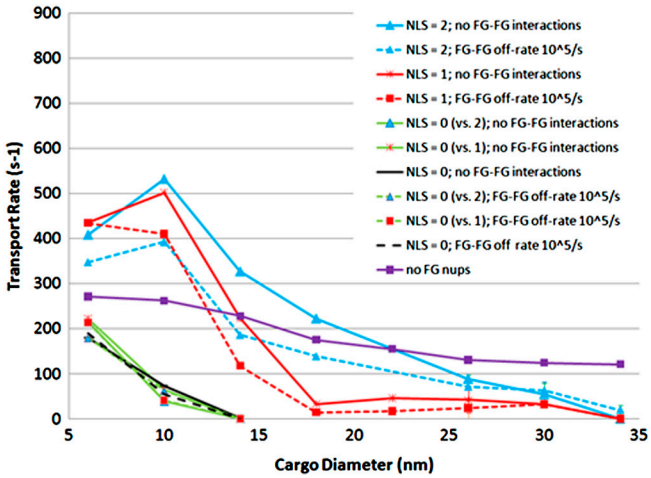

Fig. S5. Macroscopic transport rates for the 1-ring system as a function of cargo size and number of NLS tags for different FG-FG off-rates for FG-Nup filaments with mean end-to-end distance = 24 ± 8 nm (Ctheta = 0.002).

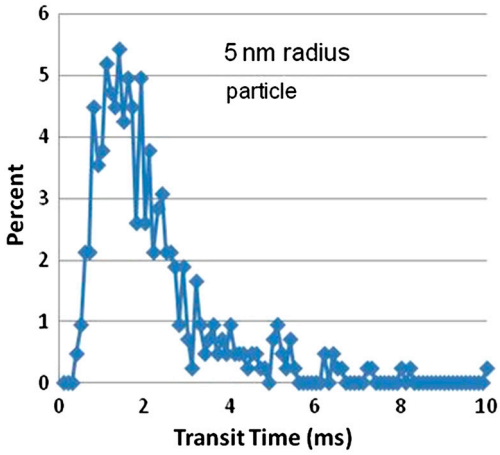

Fig. S6. Sample histogram of the transit times for 10-nm diameter cargo with 1 NLS (1-ring system, no FG-FG interactions, Ctheta = 0.02).

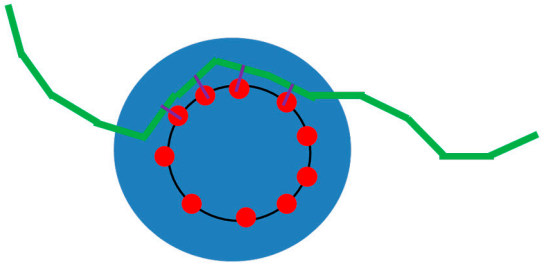

Fig. S7. Schematic of cargo-kap-FG binding. Cargo is represented by the blue sphere. The virtual karyopherin is represented by the black ring and features 10 FG binding sites (red spheres). The FG-Nup filament (green) is comprised of segments. Kap-FG bonds are represented by the purple lines.

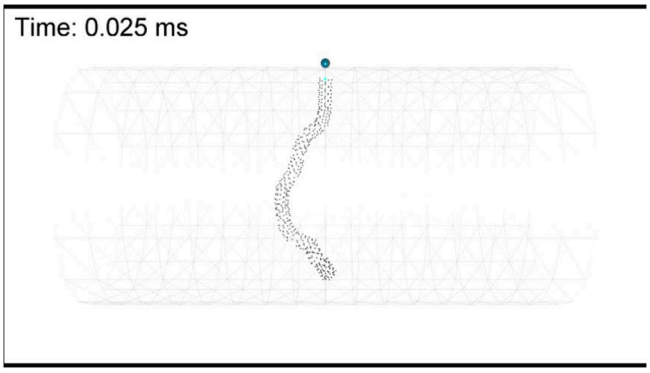

Movie S1. Dynamics of a single FG-Nup filament anchored to the inner rim of the model NPC (filament radius 3 nm, length 55 nm, Ctheta = 0.002).

Movie S1 (WMV)

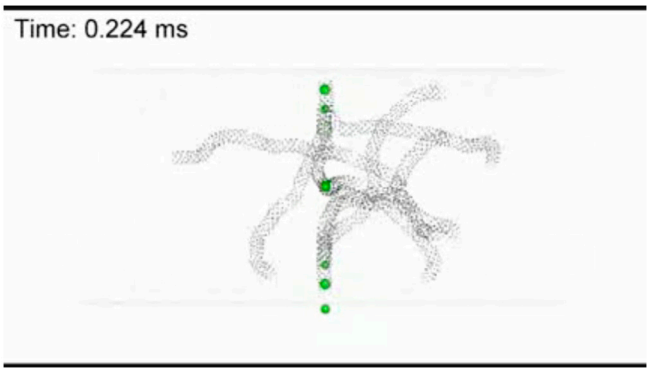

Movie S2. FG-Nup dynamics were simulated in a NPC model system with 1 ring of 8 FG-Nups. Each Nup is 55 nm long, with 13 FG repeats spaced along its length. The FG-FG off rate is 10^{∞}/s, whereas Ctheta = 0.02.

Movie S2 (MOV)

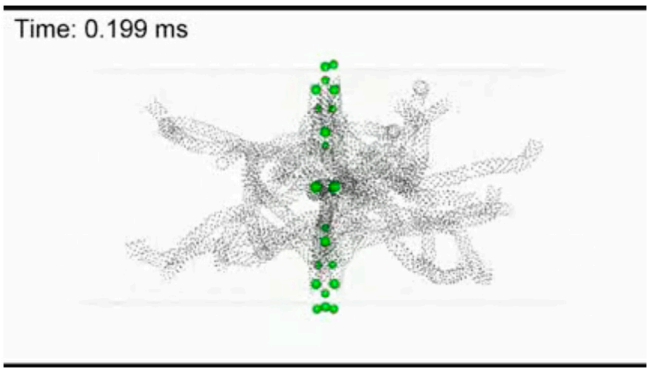

Movie S3. FG-Nup dynamics were simulated in a NPC model system with 3 rings of 8 FG-Nups each for a total of 24 FG-Nups, spaced 1.78 nm apart and with adjacent rings rotated 22.5° with respect to each other. Each Nup is 55 nm long, with 13 FG repeats spaced along its length. The FG-FG off rate is 10^{∞}/s, whereas Ctheta = 0.02.

Movie S3 (MOV)

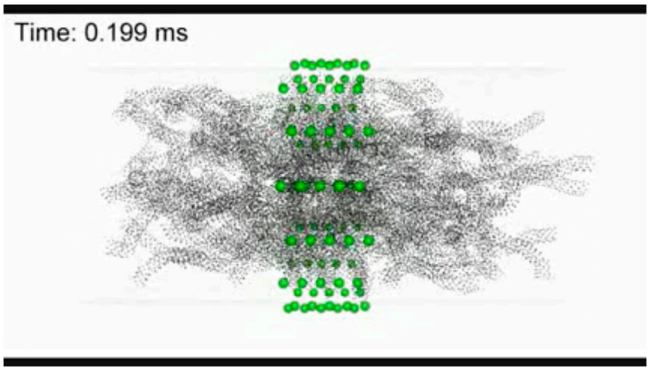

Movie S4. FG-Nup dynamics were simulated in a NPC model system with 10 rings of 8 FG-Nups each for a total of 80 FG-Nups, spaced 1.78 nm apart and with adjacent rings rotated 22.5° with respect to each other. Each Nup is 55 nm long, with 13 FG repeats spaced along its length. The FG-FG off rate is 10^{∞}/s, whereas Ctheta = 0.02.

Movie S4 (MOV)

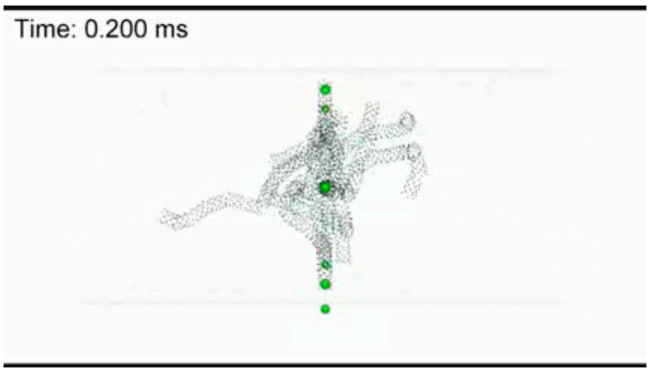

Movie S5. FG-Nup dynamics were simulated in a NPC model system with 1 ring of 8 FG-Nups. Each Nup is 55 nm long, with 13 FG repeats spaced along its length. The FG-FG off rate is 10^4/s, whereas Ctheta = 0.02.

Movie S5 (MOV)

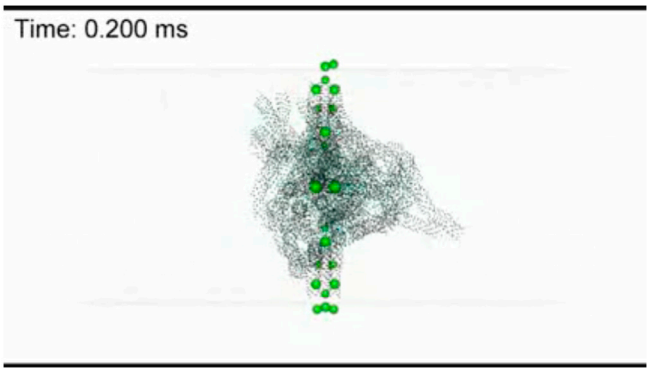

Movie S6. FG-Nup dynamics were simulated in a NPC model system with 3 rings of 8 FG-Nups each for a total of 24 FG-Nups, spaced 1.78 nm apart and with adjacent rings rotated 22.5° with respect to each other. Each Nup is 55 nm long, with 13 FG repeats spaced along its length. The FG-FG off rate is 10^4/s, whereas Ctheta = 0.02.

Movie S6 (MOV)

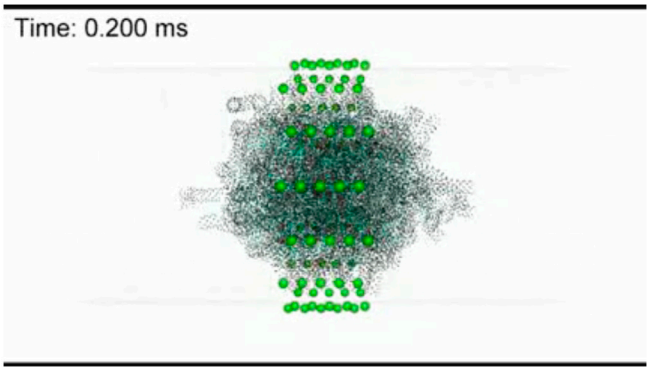

Movie S7. FG-Nup dynamics were simulated in a NPC model system with 10 rings of 8 FG-Nups each for a total of 80 FG-Nups, spaced 1.78 nm apart and with adjacent rings rotated 22.5° with respect to each other. Each Nup is 55 nm long, with 13 FG repeats spaced along its length. The FG-FG off rate is 10^4/s, whereas Ctheta = 0.02.

Movie S7 (MOV)

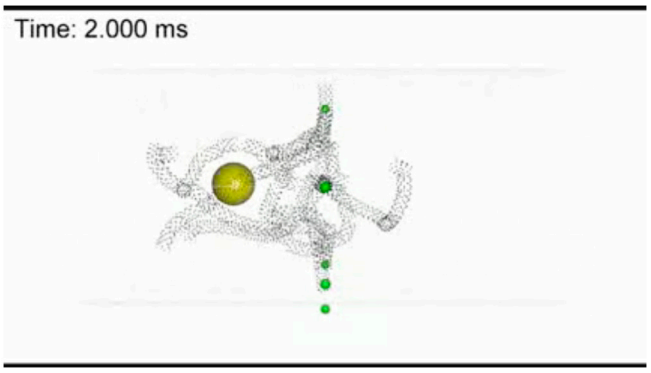

Movie S8. Cargo transport was simulated in the 1-ring NPC model system with FG-FG off rate 10^{∞}/s and Ctheta = 0.02. Each cargo is 10-nm diameter. Cargo with one NLS are colored red, whereas cargo without NLS are colored yellow. One of the NLS cargo is colored green to facilitate following its trajectory.
Movie S8 (MOV)

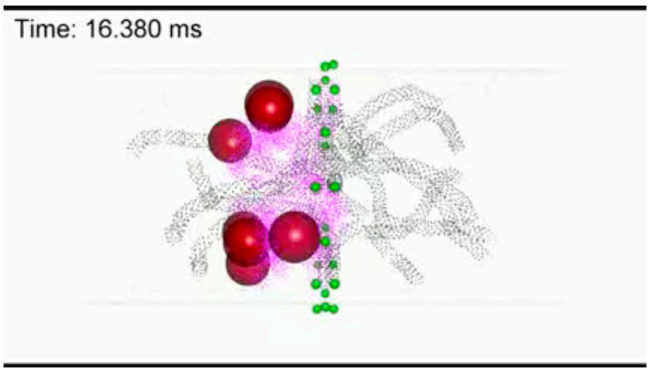

Movie S9. Cargo transport was simulated in the 3-ring NPC model system with FG-FG off rate 10^{∞}/s and Ctheta = 0.02. Each cargo is 10-nm diameter. Cargo with one NLS are colored red, whereas cargo without NLS are colored yellow. The green cargo has one NLS and corresponds to the trajectory analyzed in Fig. 4 *A* and *B*.
Movie S9 (MOV)

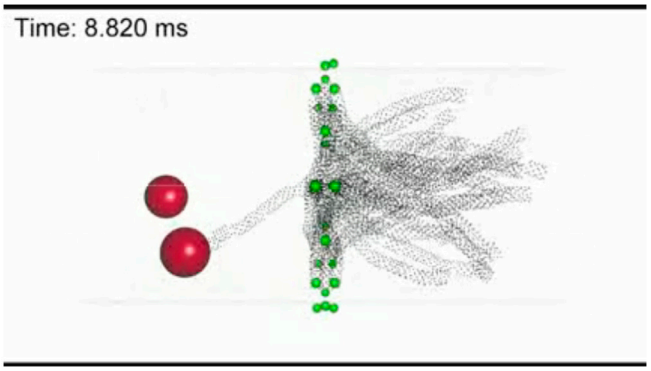

Movie S10. Cargo transport was simulated in the 3-ring NPC model system with FG-FG off rate 10^{∞}/s and Ctheta = 0.2. Each cargo is 10-nm diameter. Cargo with one NLS are colored red, whereas cargo without NLS are colored yellow. The green cargo has one NLS and corresponds to the trajectory analyzed in Fig. S3*C*.
Movie S10 (MOV)

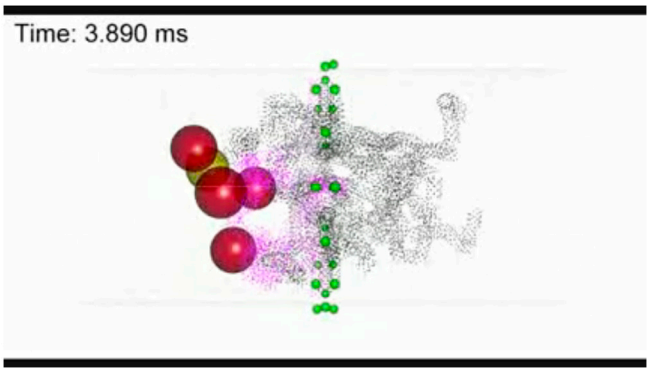

Movie S11. Cargo transport was simulated in the 3-ring NPC model system with FG-FG off rate 10^{∞}/s and Ctheta = 0.002. Each cargo is 10-nm diameter. Cargo with one NLS are colored red, whereas cargo without NLS are colored yellow. The green cargo has one NLS and corresponds to the trajectory analyzed in Fig. S3*B*.
Movie S11 (MOV)

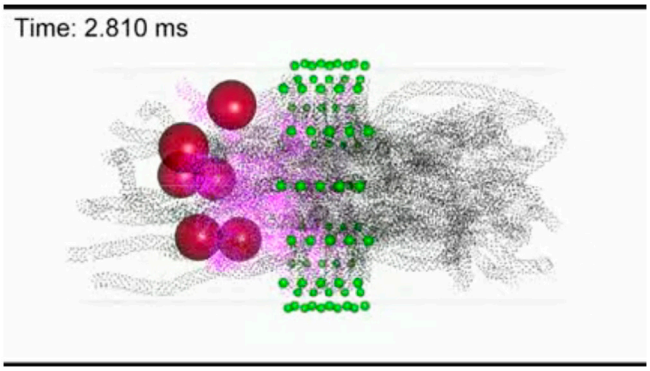

Movie S12. Cargo transport was simulated in the 10-ring NPC model system with FG-FG off-rate 10^{∞}/s and Ctheta = 0.02. Each cargo is 10-nm diameter. Cargo with 1 NLS are colored red, while cargo without NLS are colored yellow. The green cargo has 1 NLS and corresponds to the trajectory analyzed in Fig. S3*A*.
Movie S12 (MOV)

Table S1. Macroscopic transport rates (cargo per second) for the 3-ring system with 1.2-nm FG-Nup filament radius, Ctheta = 0.02 (standard error in parentheses)

	FG-FG off rate 10^{∞}/s					FG-FG off rate 10^{5}/s				
Cargo diameter, nm	NLS 1 v. 0	NLS 0 v. 1	NLS 2 v. 0	NLS 0 v. 2	NLS 0	NLS 1 v. 0	NLS 0 v. 1	NLS 2 v. 0	NLS 0 v. 2	NLS 0
6	1096 (1)	183 (0.9)	994 (0.5)	130 (0.2)	201 (0.7)	449 (0.7)	132 (0.8)	434 (0.4)	94 (0.3)	152 (0.6)
18	669 (1)	0 (0)	1241 (1)	0 (0)		0.5 (0.02)	0 (0)	127 (0.4)	0 (0)	

Rate generally increases with number of NLS tags (especially for larger cargo) and decreases with increased FG-FG interactions as well as cargo size. Non-NLS cargo (NLS 0) rates are essentially unaffected by the presence of NLS cargo with one NLS tag (NLS 0 versus 1), though 2 tags (NLS 0 versus 2) does decrease rate somewhat.

Table S2. Macroscopic transport rates and mean transit times for the 10-ring system (cargo diameter 10 nm, NLS = 1, FG-Nup radius 3 nm, Ctheta = 0.02) (standard error in parentheses)

	FG-FG off rate 10^{∞}/s	FG-FG off rate 10^{5}/s
Rate per second	325 (1)	114 (1)
Mean transit time, ms	27 (4)	35 (7)